



Article

The Impact of Systematic Attitude Error on the Measurement of Interferometric Radar Altimeter

Haoyan Tang ¹, Yunhua Wang ^{1,2,*}, Chaofang Zhao ^{1,2}, Daozhong Sun ¹, Ge Chen ^{1,2} and Hanwei Sun ³¹ Faculty of Information Science and Engineering, Ocean University of China, Qingdao 266100, China² Pilot National Laboratory for Marine Science and Technology, Qingdao 266237, China³ Beijing Institute of Radio Measurement, Beijing 100854, China

* Correspondence: yunhuawang@ouc.edu.cn

Abstract: Altimetric error has always been the significant performance parameter of the interferometric radar altimeter (IRA), particularly in the observation of sub-mesoscale ocean dynamic processes in which a higher accuracy of sea surface elevation (SSE) measurement is needed. The systematic attitude error of IRA associated with platform altitude, roll, pitch, and yaw errors is a remarkable source of altimetric error. However, the coupling attitude altimetric error is still less discussed up to now. In this paper, we focus on the study of the coupling attitude altimetric error and its related position-shifting, which are all induced by the attitude errors. The theoretical formulas of the coupling attitude altimetric error were derived, and the theoretical analysis demonstrates that the coupling attitude altimetric error is no longer along the range direction of the IRA image rigorously due to the change of the radar beam pointing. Based on theoretical formulas proposed by this study, the coupling attitude altimetric error and its related position-shifting are simulated and verified by using attitude data recorded by an airborne position and orientation system (POS) of three airborne experiments. The experimental results illustrate that the simulated coupling attitude altimetric errors are consistent with the measurements of the airborne experiments.



Citation: Tang, H.; Wang, Y.; Zhao, C.; Sun, D.; Chen, G.; Sun, H. The Impact of Systematic Attitude Error on the Measurement of Interferometric Radar Altimeter. *Remote Sens.* **2022**, *14*, 6028. <https://doi.org/10.3390/rs14236028>

Academic Editor: Carlos López-Martínez

Received: 24 October 2022

Accepted: 25 November 2022

Published: 28 November 2022

Publisher's Note: MDPI stays neutral with regard to jurisdictional claims in published maps and institutional affiliations.



Copyright: © 2022 by the authors. Licensee MDPI, Basel, Switzerland. This article is an open access article distributed under the terms and conditions of the Creative Commons Attribution (CC BY) license (<https://creativecommons.org/licenses/by/4.0/>).

Keywords: interferometric radar altimeter; coupling attitude altimetric error; airborne experiments; sea surface elevation measurement

1. Introduction

One of the purposes of the interferometric radar altimeter (IRA) is to observe the sub-mesoscale ocean dynamic processes with centimeter-level absolute accuracy in a wide-swath of ~100 km or wider [1]. The limited resolution of current altimeter systems has prevented the study of sub-mesoscale eddy processes that are critical to understanding the ocean's roles in Earth's climate [2]. The Surface Water and Ocean Topography (SWOT) to be launched this year and the proposed Guanlan satellite missions both belonged to this new generation of altimeter [3–8], and both missions will provide the data of SSE with a high spatial resolution (~15 km) and wide-swath (~150 km) data of sea surface elevation. Prior to that, the SARIn mode of CryoSat-2 was specifically designed to improve the data quality over the polar regions. As the first satellite equipped with the synthetic aperture interferometric radar altimeters (SIRAL), the in-flight CryoSat-2 was designed to be able to map broad (5 km-wide) swaths of surface elevation with fine (500 m) spatial resolution. The SARIn mode of this nadir-looking altimeter is a positive exploration of the IRA development [9–12]. For the observation of sub-mesoscale ocean phenomena, a great challenge to the accuracy and reliability of the new generation of altimeters is posed. The altimetric errors are contained in the full link of electromagnetic wave propagation from the altimeter system to sea surface scattering, which are difficult to be resolved either by physical or algorithmic methods. In SWOT, in order to achieve the desired measurement accuracy, the altimetric errors have been divided into three main categories: ocean media/wave error requirements, ocean random error requirements, and ocean

systematic error requirements [13,14]. The instrument's systematic error includes systematic attitude error (roll, yaw, and pitch), orbit's altitude error, baseline length error, phase measurement error, and system time delay error. Consequently, any slight change in the altimeter system could have a significant impact on the altimetry accuracy.

In the early 2000s, the basic interferometric geometric model and equations were given, and the sensitivity of parameter variations to elevation was analyzed based on mathematical partial derivatives [15–18]. Some studies focused on the analysis of the parameters that have a significant effect on altimetry, however, the combined effects of roll, pitch, and yaw in altimetry error were not considered [14,19–27]. Actually, the coupling attitude altimetric error is not a simple sum of each attitude error, and the position-shifting due to attitude errors was not considered. Our studies show that the coupling attitude altimetric error is no longer along the range direction of the IRA image rigorously after considering the position-shifting. This effect is especially remarkable as the attitude altimetric errors of the IRA system are large.

In this work, the impact of the coupling attitude altimetric error on the SSE retrieved from IRA has been investigated in detail, and the theoretical formulas for quantitatively evaluating the coupling attitude altimetric error are also derived. The validity of the theoretical formulas has been confirmed by three experiments of the airborne IRA. This paper is organized as follows: Section 2 gives the observation geometric of IRA and the theoretical formulas of the coupled altimetry error induced by the systematic attitude errors (i.e., altitude, roll, pitch, and yaw errors). The consistency of the coupling attitude altimetric error result and each single error result is compared, respectively, and, finally, the position-shifting of coupling attitude altimetric error due to attitude errors is discussed. Section 3 analyzes the rationality of the theoretical results based on three experiments of the airborne IRA carried out in the Rizhao sea area. In the last section, the main conclusions and future studies are summarized.

2. Theory of Coupling Attitude Altimetric Error of IRA

The coupling attitude altimetric error of IRA can be mainly divided into four items, i.e., platform altitude error, roll error, pitch error, and yaw error. Referring to previous studies [8,28–30], each error was discussed in terms of both SAR geometry interferometry and data processing. During SSE calculation, the interferometric phase is calculated by using the master–slave images acquired by the IRA. The interferometric phase contains the elevation phase and the flat-earth phase [31]. The SSE can be calculated by the elevation phase and the flat-earth phase needs to be removed before, which is generally referred to as flat-earth phase removal. The calculation of the flat-earth phase is based on the interferometric geometric, therefore, it can be considered that the systematic attitude errors will lead to flat-earth phase error, and, eventually, those errors transfer into the calculation of the SSE retrieved by the IRA.

2.1. Coupling Attitude Altimetric Error

Figure 1 shows the IRA geometry: the solid line represents the geometry of the ideal scenario and the dashed line represents the geometry of the scenario with coupling attitude error, in which the antenna position, the radar beam pointing position, the baseline direction, and the baseline inclination are all changed by the coupling attitude error, and, finally, the entire observation swath direction is changed as well. The coupling attitude altimetric error can be calculated by the difference between two flat-earth phases, one from the observation scenario with coupling attitude error, and the other one from the ideal observation scenario. The effect of coupling attitude error combined with platform altitude, roll, pitch, and yaw errors can be described with a transformation matrix M_ε [23,32].

$$M_\varepsilon = \begin{pmatrix} M_R & M_T \\ 0^T & 1 \end{pmatrix} \quad (1)$$

where 0^T is a 1×3 zero matrix. M_R represents the rotation matrix as in Equation (2), which is determined by the platform's roll θ_{roll} , pitch θ_{pitch} , and yaw θ_{yaw} .

$$M_R = M_{yaw}M_{pitch}M_{roll} = \begin{pmatrix} \cos \theta_{roll} \cos \theta_{yaw} + \sin \theta_{roll} \sin \theta_{yaw} \sin \theta_{pitch} & -\cos \theta_{pitch} \sin \theta_{yaw} & -\sin \theta_{roll} \cos \theta_{yaw} + \cos \theta_{roll} \sin \theta_{pitch} \sin \theta_{yaw} \\ -\cos \theta_{yaw} \sin \theta_{roll} \sin \theta_{pitch} + \cos \theta_{roll} \sin \theta_{yaw} & \cos \theta_{yaw} \cos \theta_{pitch} & -\cos \theta_{roll} \cos \theta_{yaw} \sin \theta_{pitch} - \sin \theta_{roll} \sin \theta_{yaw} \\ \sin \theta_{roll} \cos \theta_{pitch} & \sin \theta_{pitch} & \cos \theta_{roll} \cos \theta_{pitch} \end{pmatrix} \quad (2)$$

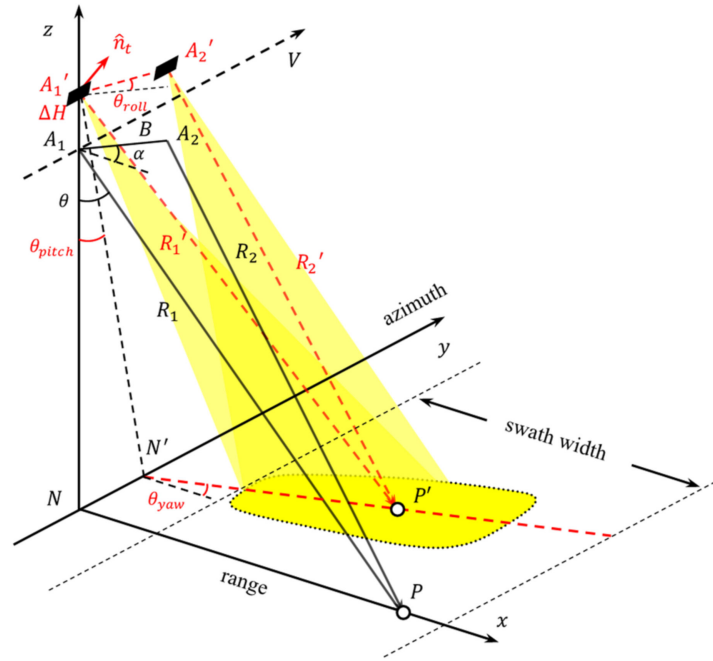


Figure 1. IRA geometry with coupling attitude altimetric error.

Generally, the attitude errors are small, therefore the small-angle approximation can be applied to Equation (2). With the cosine of the attitude angle approximated by 1 and the sine of the attitude angle approximated by the angle itself, the approximation of the rotation matrix M_R can be rewritten as in Equation (3) after ignoring the higher-order terms.

$$M_R \approx \begin{pmatrix} 1 & -\theta_{yaw} & -\theta_{roll} \\ \theta_{yaw} & 1 & -\theta_{pitch} \\ \theta_{roll} & \theta_{pitch} & 1 \end{pmatrix} \quad (3)$$

M_T represents the rotation matrix caused by platform altitude error.

$$M_T = (0 \ 0 \ \Delta H)^T \quad (4)$$

where ΔH is platform altitude error.

In Figure 1, a right-hand system of Cartesian coordinates is established with point N as the origin of the coordinate, the cross-track direction (range direction) as the x -axis, the along-track direction (azimuth direction) as the y -axis, and the elevation direction as the z -axis. The location of the radar master antenna A_1 is set at $(0, 0, R_1 \cos \theta)$, and to make the analysis process clearer, the observed target is located in $P = (R_1 \sin \theta, 0, 0)$. R_1 is the ideal slant range of the master antenna to the target and is set to satisfy an important constraint that it should remain the same in any scenario. θ is the incident angle and $R_1 \cos \theta = H$, and H is the platform altitude. The location of the slave antenna A_2 is described as $(B \cos \alpha, 0, R_1 \cos \theta + B \sin \alpha)$, B is the length of baseline vector $\overrightarrow{A_1A_2}$, and α is the baseline angle in the original plane A_1PA_2 . The normal vector of plane A_1PA_2 is $\hat{n} = (0, 1, 0)$, so the equation of plane A_1PA_2 can be expressed as $y = 0$. Due to the attitude

errors, the antenna beam pointing location is changed from P to P' , therefore the plane A_1PA_2 will transform into $A_1'P'A_2'$, and then the location of the master antenna A_1' is easy to get, as in Equation (5).

$$A_1' = (0, 0, R_1 \cos \theta + \Delta H) \tag{5}$$

Using the approximated rotation matrix, the normal vector \hat{n} of plane $A_1'P'A_2'$ changes into \hat{n}_t as in Equation (6).

$$\hat{n}_t = \frac{M_R \cdot \hat{n}^T}{|M_R \cdot \hat{n}^T|} = \frac{1}{\sqrt{1 + \theta_{yaw}^2 + \theta_{pitch}^2}} \begin{pmatrix} -\theta_{yaw} \\ 1 \\ \theta_{pitch} \end{pmatrix} \tag{6}$$

Using the normal vector \hat{n}_t , the equation of plane $A_1'P'A_2'$ with coupling attitude error can be given:

$$-\theta_{yaw}x + y + \theta_{pitch}z - \theta_{pitch}(H + \Delta H) = 0 \tag{7}$$

The baseline vector $\overrightarrow{A_1'A_2'}$ with coupling attitude error can be obtained by left-multiplication of the transformation matrix M_ϵ with the vector $\overrightarrow{A_1A_2}$ and expressed in Equation (8):

$$\begin{pmatrix} \overrightarrow{A_1'A_2'} \\ 1 \end{pmatrix} = M_\epsilon \begin{pmatrix} \overrightarrow{A_1A_2} \\ 1 \end{pmatrix}^T \tag{8}$$

thus, the location of antenna A_2' can be written in Equation (9),

$$A_2' = \begin{pmatrix} B(\cos \alpha - \theta_{roll} \sin \alpha), \\ B(\theta_{yaw} \cos \alpha - \theta_{pitch} \sin \alpha), \\ H + \Delta H + B(\theta_{roll} \cos \alpha + \sin \alpha) \end{pmatrix} \tag{9}$$

There are two constraints of the new position P' , one is that it should be located in the plane $A_1'P'A_2'$, and the other one is that the R_1 is invariant. The coordinate of P' is calculated as:

$$P' = \left((H + \Delta H) \sqrt{\frac{\left(\frac{R_1}{H + \Delta H}\right)^2 - \theta_{pitch}^2 - 1}{1 + \theta_{yaw}^2}}, (H + \Delta H) \left(\theta_{pitch} + \theta_{yaw} \sqrt{\frac{\left(\frac{R_1}{H + \Delta H}\right)^2 - \theta_{pitch}^2 - 1}{1 + \theta_{yaw}^2}} \right), 0 \right) \tag{10}$$

From the slant-ranges R_1 , the coordinate of the slave antenna A_2' and target P' , the flat-earth phase φ_{flat_errors} with coupling attitude error can be calculated by Equation (11).

$$\varphi_{flat_errors} = -\frac{2\pi}{\lambda} \left(\left| \overrightarrow{A_1'P'} \right| - \left| \overrightarrow{A_2'P'} \right| \right) = -\frac{2\pi}{\lambda} (R_1 - R_2') \approx \frac{2\pi}{\lambda} B \frac{H + \Delta H}{R_1} \left[\begin{matrix} \cos \alpha \left(\theta_{roll} - \sqrt{(1 + \theta_{yaw}^2) \left(\left(\frac{R_1}{H + \Delta H}\right)^2 - \theta_{pitch}^2 - 1} \right)} \right) \\ + \sin \alpha \left(1 + \theta_{roll} \sqrt{\frac{\left(\frac{R_1}{H + \Delta H}\right)^2 - \theta_{pitch}^2 - 1}{1 + \theta_{yaw}^2}} \right) \end{matrix} \right] \tag{11}$$

The ideal flat-earth phase φ_{flat} can be calculated by Equation (12).

$$\varphi_{flat} = -\frac{2\pi}{\lambda} (R_1 - R_2) = -\frac{2\pi}{\lambda} \left(\left| \overrightarrow{A_1P} \right| - \left| \overrightarrow{A_2P} \right| \right) \approx \frac{2\pi}{\lambda} B \sin(\alpha - \theta) \tag{12}$$

According to the interferometric imaging theory, the coupling attitude altimetric error can be calculated by Equation (13).

$$\Delta H_{errors} = -\frac{\lambda R_1 \sin \theta}{2\pi B \cos(\alpha - \theta)} (\varphi_{flat_errors} - \varphi_{flat}) = -\frac{R_1 \sin \theta}{\cos(\alpha - \theta)} \left\{ \frac{H + \Delta H}{R_1} \left[\begin{array}{l} \cos \alpha \left(\theta_{roll} - \sqrt{(1 + \theta_{yaw}^2) \left(\left(\frac{R_1}{H + \Delta H} \right)^2 - \theta_{pitch}^2} - 1 \right)} \right) \\ + \sin \alpha \left(1 + \theta_{roll} \sqrt{\frac{\left(\frac{R_1}{H + \Delta H} \right)^2 - \theta_{pitch}^2}{1 + \theta_{yaw}^2}} \right) \end{array} \right] - \sin(\alpha - \theta) \right\} \quad (13)$$

Equation (13) shows that the result is not a simple summation of each attitude altimetric error, but the coupling result of the four attitude errors, which makes the variation characteristics of the altimetry error difficult to determine directly.

2.2. Independent Analysis of Attitude Errors

Independent analyses of the attitude errors can reveal the impact of each attitude error on the measurement, and these impacts have been discussed in related studies [19–27]. To further discuss the correctness of the coupling attitude altimetric error, a similar approach is used to analyze each attitude error and the results are compared with the degeneration result of Equation (13). In each subfigure of Figure 2, the ideal scenario is drawn in the solid lines, and the scenario with each attitude error is in dashed lines.

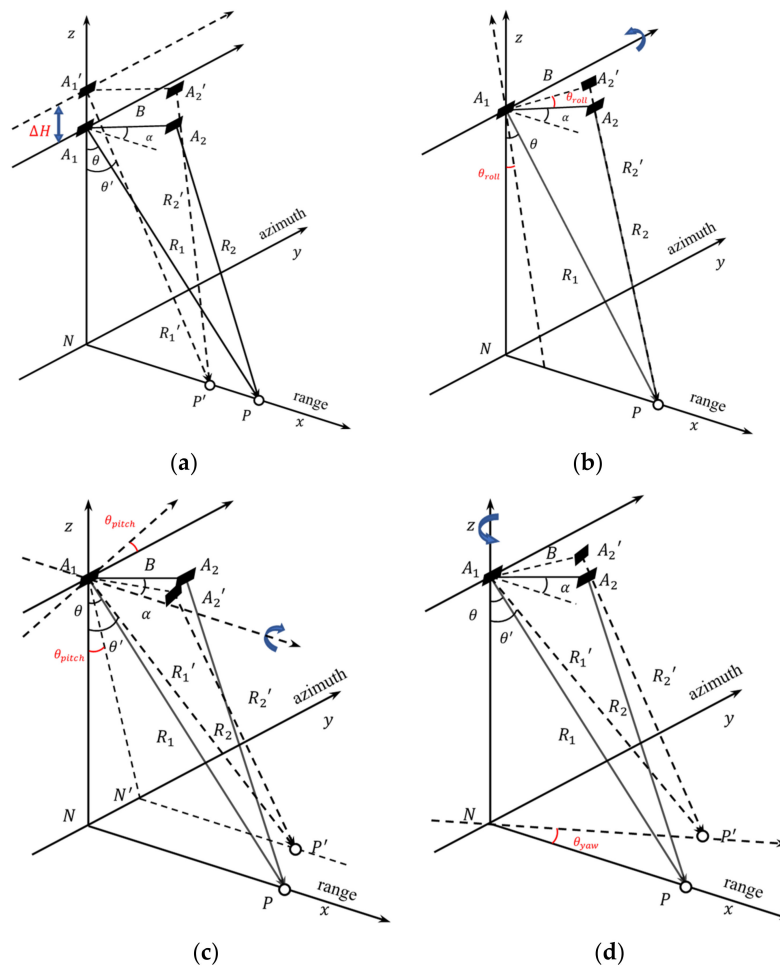


Figure 2. IRA geometry with four attitude errors. (a) Platform altitude error. (b) Roll error. (c) Pitch error. (d) Yaw error.

2.2.1. Platform Altitude Error

In the geometric model with platform altitude error plot in Figure 2a, the altitude changes from H to $H + \Delta H$ due to the altitude error. Supposing the baseline angle and the

slant-range between the target and the master antenna keep no change, the changed radar beam will point to the position of P' from P ,

$$P' = \left(R_1 \sqrt{1 - \left(\cos \theta + \frac{\Delta H}{R_1} \right)^2}, 0, 0 \right) \quad (14)$$

Thus, the flat-earth phase $\varphi_{flat_altitude_error}$ in the observing scenario with altitude error can be calculated by Equation (15).

$$\begin{aligned} \varphi_{flat_altitude_error} &= -\frac{2\pi}{\lambda} (R_1' - R_2') \\ &\approx \frac{2\pi}{\lambda} B \sin(\alpha - \theta') \end{aligned} \quad (15)$$

where θ' is the incident angle with altitude error, which satisfied $\cos \theta' = \cos \theta + \frac{\Delta H}{R_1}$, and the slant range of the master antenna satisfied $R_1 = R_1'$. According to Equation (12), the altimetric error can be calculated as Equation (16),

$$\begin{aligned} \Delta h_{altitude_error} &= -\frac{\lambda R_1 \sin \theta}{2\pi B \cos(\alpha - \theta)} \left(\varphi_{flat_altitude_error} - \varphi_{flat} \right) \\ &\approx -\Delta H \end{aligned} \quad (16)$$

Compared with the coupling attitude altimetric error in Equation (13), when only the platform altitude error is considered, the degradation of Equation (13) can be written by Equation (17), which is consistent with Equation (16), and the altimetric error caused by platform altitude error is approximately equal to itself ΔH in amplitude.

$$\Delta h_{errors_ \Delta H} \Big|_{\substack{\theta_{roll} = 0 \\ \theta_{pitch} = 0 \\ \theta_{yaw} = 0}} = -\frac{R_1 \sin \theta}{\cos(\alpha - \theta)} \cdot \left[\frac{\Delta H}{R_1} \sin \alpha + \cos \alpha \sin \theta \left(1 - \sqrt{1 - \left(\frac{\Delta H}{R_1 \sin \theta} \right)^2 - 2 \frac{\Delta H \cos \theta}{R_1 \sin^2 \theta}} \right) \right] \approx -\Delta H \quad (17)$$

This error varies only along the azimuth direction but does not change with the range distance of the swath.

2.2.2. Roll Error

Supposing the roll angle of the platform is θ_{roll} as shown in Figure 2b, which causes the rotation of the baseline vector around the y -axis, and the radar beam still points to the position P , the flat-earth phase $\varphi_{flat_roll_error}$ with roll error can be expressed in Equation (18). With the ideal flat-earth phase from Equation (12), the altimetry error can be calculated using Equations (18) and (19),

$$\begin{aligned} \varphi_{flat_roll_error} &= -\frac{2\pi}{\lambda} (R_1 - R_2') \\ &\approx -\frac{2\pi}{\lambda} B \sin(\alpha + \theta_{roll} - \theta), \end{aligned} \quad (18)$$

$$\begin{aligned} \Delta h_{roll_error} &= -\frac{\lambda R_1 \sin \theta}{2\pi B \cos(\alpha - \theta)} \left(\varphi_{flat_roll_error} - \varphi_{flat} \right) \\ &\approx -R_1 \sin \theta \cdot \theta_{roll} \end{aligned} \quad (19)$$

Compared with the coupling attitude altimetric error in Equation (13), when only the roll error is considered, the degradation of Equation (13) can be written by Equation (20),

$$\Delta h_{errors_ \theta_{roll}} \Big|_{\substack{\Delta H = 0 \\ \theta_{pitch} = 0 \\ \theta_{yaw} = 0}} = -R_1 \sin \theta \cdot \theta_{roll} \quad (20)$$

The result is consistent with Equation (19), and the altimetric error caused by roll error increases across the swath. This altimetric error varies both along the azimuth and the range direction.

2.2.3. Pitch Error

Supposing the pitching angle of platform is θ_{pitch} as shown in Figure 2c, which causes the rotation of the baseline vector around the x -axis and the translation of the swath from line NP to $N'P'$, the position P' can be written as in Equation (21),

$$P' \approx \left(R_1 \sqrt{1 - \cos^2 \theta (1 + \theta_{pitch}^2)}, H \cdot \theta_{pitch}, 0 \right) \tag{21}$$

According to the geometry relationship, the only thing that changed is the angle between the slant range and the baseline vector, the slant range of the slave antenna R_2' can be calculated as in Equation (22),

$$R_2' \approx \sqrt{\left(R_1 \sqrt{1 - \cos^2 \theta (1 + \theta_{pitch}^2)} - B \cos \alpha \right)^2 + \left(H \cdot \theta_{pitch} + B \sin \alpha \cdot \theta_{pitch} \right)^2 + (-H - B \sin \alpha)^2} \tag{22}$$

The flat-earth phase with pitch error $\varphi_{flat_pitch_error}$ can be calculated using Equation (23):

$$\begin{aligned} \varphi_{flat_pitch_error} &= -\frac{2\pi}{\lambda} (R_1' - R_2') \\ &\approx \frac{2\pi}{\lambda} B \left(\frac{\cos \theta \sin \alpha}{\cos \theta_{pitch}} - \cos \alpha \sqrt{1 - \cos^2 \theta (1 + \tan^2 \theta_{pitch})} \right) \end{aligned} \tag{23}$$

Using the ideal flat-earth phase from Equation (12), the altimetric error can be calculated by Equation (24).

$$\Delta h_{pitch_error} = -\frac{\lambda R_1 \sin \theta}{2\pi B \cos(\alpha - \theta)} (\varphi_{flat_pitch_error} - \varphi_{flat}) \approx -\frac{H}{2} \cdot \theta_{pitch}^2 \tag{24}$$

Compared with the coupling attitude altimetric error in Equation (13), when only the pitch error is considered, the degradation of Equation (13) can be written by Equation (25).

$$\begin{aligned} \Delta h_{errors_pitch} \Big|_{\substack{\Delta H = 0 \\ \theta_{roll} = 0 \\ \theta_{yaw} = 0}} &\approx -\frac{H \cos \theta \cos \alpha}{2 \cos(\alpha - \theta)} \theta_{pitch}^2 \\ &\approx -\frac{H}{2} \theta_{pitch}^2 \end{aligned} \tag{25}$$

The result is consistent with Equation (24), which indicates that the altimetric error caused by pitch error is approximately proportional to the platform altitude and the square of pitch error, the error does not change with the range distance of the swath, which is the same as the platform altitude error.

2.2.4. Yaw Error

Supposing the yaw angle of the platform is θ_{yaw} as shown in Figure 2d, which causes the rotation of the baseline vector around the z -axis and the rotation of swath from the direction of line NP to $N'P'$, the changed radar beam will point to position P' from P . As all vectors are rotated only, none of the vector values change, therefore, the altimetric error due to yaw error should be zero:

$$\Delta h_{yaw_error} = -\frac{\lambda R_1 \sin \theta}{2\pi B \cos(\alpha - \theta)} (\varphi_{flat_yaw_error} - \varphi_{flat}) = 0 \tag{26}$$

Compared with the coupling attitude altimetric error in Equation (13), when only the yaw error is considered, the degradation of Equation (13) can be written by Equation (27).

$$\Delta h_{errors_yaw} \Big|_{\substack{\Delta H = 0 \\ \theta_{roll} = 0 \\ \theta_{pitch} = 0}} \approx -\frac{R_1 \sin^2 \theta \cos \alpha}{\cos(\alpha - \theta)} \frac{\theta_{yaw}^2}{2(1 + \theta_{yaw}^2)} \approx 0 \quad (27)$$

The result is consistent with Equation (26). The contribution of yaw error to the coupling attitude altimetric error can also be ignored when considering the high-order approximation in Equation (27).

After comparing the consistency of the result of coupling attitude altimetric error with results of platform altitude error, roll error, pitch error, and yaw error, the feasibility of the derivation of the coupling attitude altimetric error is confirmed.

2.3. Position-Shifting of Altimetric Error

The altimetric error induced by roll error is generally considered to be along the range direction of the IRA image [13,19,24]. However, the airborne IRA experiment results show that the altimetric error is no longer strictly along the range direction when the pitch or the yaw error also occurs. The position-shifting of the altimetric error is one of the important error sources for altimetry, although it is less discussed up to now. As shown in Figure 1, the radar beam will point to the position P' due to the attitude errors, and the swath direction \overrightarrow{NP} will change to the direction of vector $\overrightarrow{N'P'}$. It can be known from Equation (13) that the coupling attitude altimetric error is a function of the slant range R and the incidence angle θ , and these two parameters vary along the range direction of the swath. Therefore, the coupling attitude altimetric error also varies along the direction of $\overrightarrow{N'P'}$. Based on geometric analysis of the position-shifting of the altimetric error caused by coupling attitude errors, the shift can be described as the difference of coordinates in a Cartesian coordinate system due to the change of the plane where the radar beam is located and the slant-ranges as shown in Equation (28).

$$\begin{aligned} (\Delta x, \Delta y) &= (x_{P'} - x_P, y_{P'} - y_P) \\ &\approx \left((H + \Delta H) \sqrt{\frac{\left(\frac{R_1}{H + \Delta H}\right)^2 - \theta_{pitch}^2 - 1}{1 + \theta_{yaw}^2}} - R_1 \sin \theta, (H + \Delta H) \left(\theta_{pitch} + \theta_{yaw} \sqrt{\frac{\left(\frac{R_1}{H + \Delta H}\right)^2 - \theta_{pitch}^2 - 1}{1 + \theta_{yaw}^2}} \right) \right) \end{aligned} \quad (28)$$

where Δx is the shift in the range direction, and Δy is the shift in the azimuth direction. The position-shifting of altimetric error is associated with the platform altitude error, pitch error, and yaw error, but not with the roll error. When considering the platform altitude error only, the position-shifting is determined by Equation (29), and the variation of the result is only in the range direction.

$$(\Delta x, \Delta y)_{\Delta H} \approx \left(-\frac{\Delta H}{\tan \theta}, 0 \right) \quad (29)$$

When considering the pitch error only, the position-shifting determined by Equation (30), and the distribution of the result is two-dimensional.

$$(\Delta x, \Delta y)_{pitch} \approx \left(-\frac{H}{2 \tan \theta} \theta_{pitch}^2, H \theta_{pitch} \right) \quad (30)$$

When considering the yaw error only, the position-shifting determined by Equation (31), and the distribution of the result is two-dimensional.

$$(\Delta x, \Delta y)_{yaw} \approx \left(R_1 \sin \theta \frac{\theta_{yaw}^2}{2(1 + \theta_{yaw}^2)}, R_1 \sin \theta \frac{\theta_{yaw}}{\sqrt{1 + \theta_{yaw}^2}} \right) \quad (31)$$

The result illustrates that the position-shifting changes the spatial distribution of the coupling attitude altimetric error, which makes the error vary not only along the range direction of the image but also along the azimuth direction. According to the above analysis, both pitch and yaw errors will cause position-shifting in the azimuth direction. The position-shifting in the range direction is caused by these three errors, but it is much smaller than the position-shifting in the azimuth direction.

3. Simulation of Coupling Attitude Altimetric Error and Validation by Airborne IRA Experimental Data

This paper will use three data sets of airborne IRA experiments which were acquired from the Rizhao sea area, China. The experimental area is shown in Figure 3a, and the three data sets named RZ14, RZ16, and RZ24 were retrieved on 14, 16, and 24 November 2019, respectively. Three flight tracks are marked in Figure 3b, and the flight tracks of data RZ14 (blue line) and data RZ16 (black line) cross around the buoy location (pink marker), and the flight tracks of data RZ16 (black line) and RZ24 (red line) are parallel.

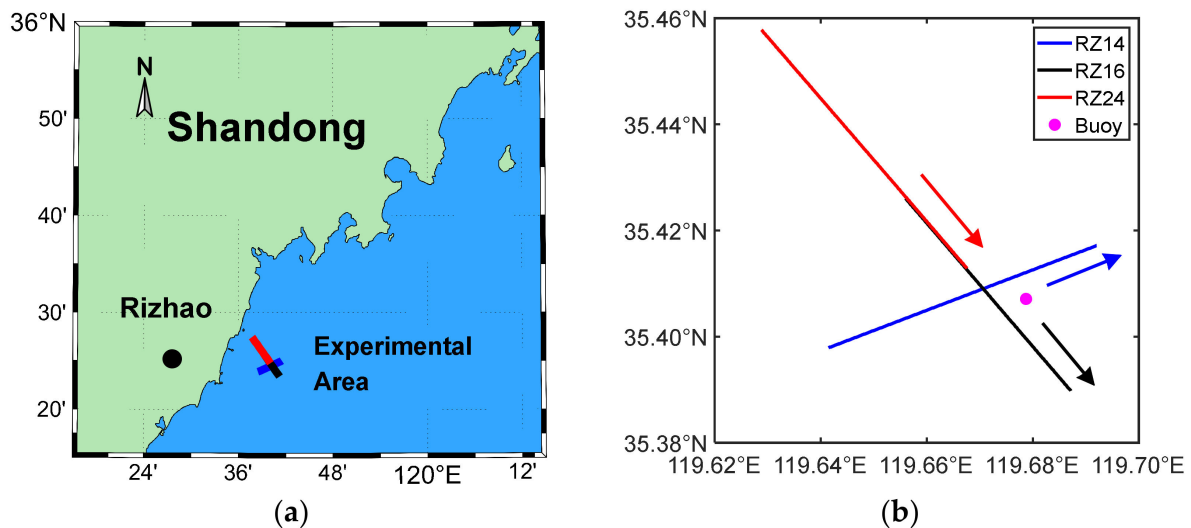


Figure 3. (a) Rizhao sea experimental area. (b) Flight tracks.

The aircraft carried a Ka and Ku dual-band IRA and the platform parameters are shown in Table 1. The original systematic attitude data of the aircraft were recorded by the POS, and the specifications of the POS_AV610 from the *Applanix* Company are shown in Table 2.

Table 1. Master parameters of the airborne system.

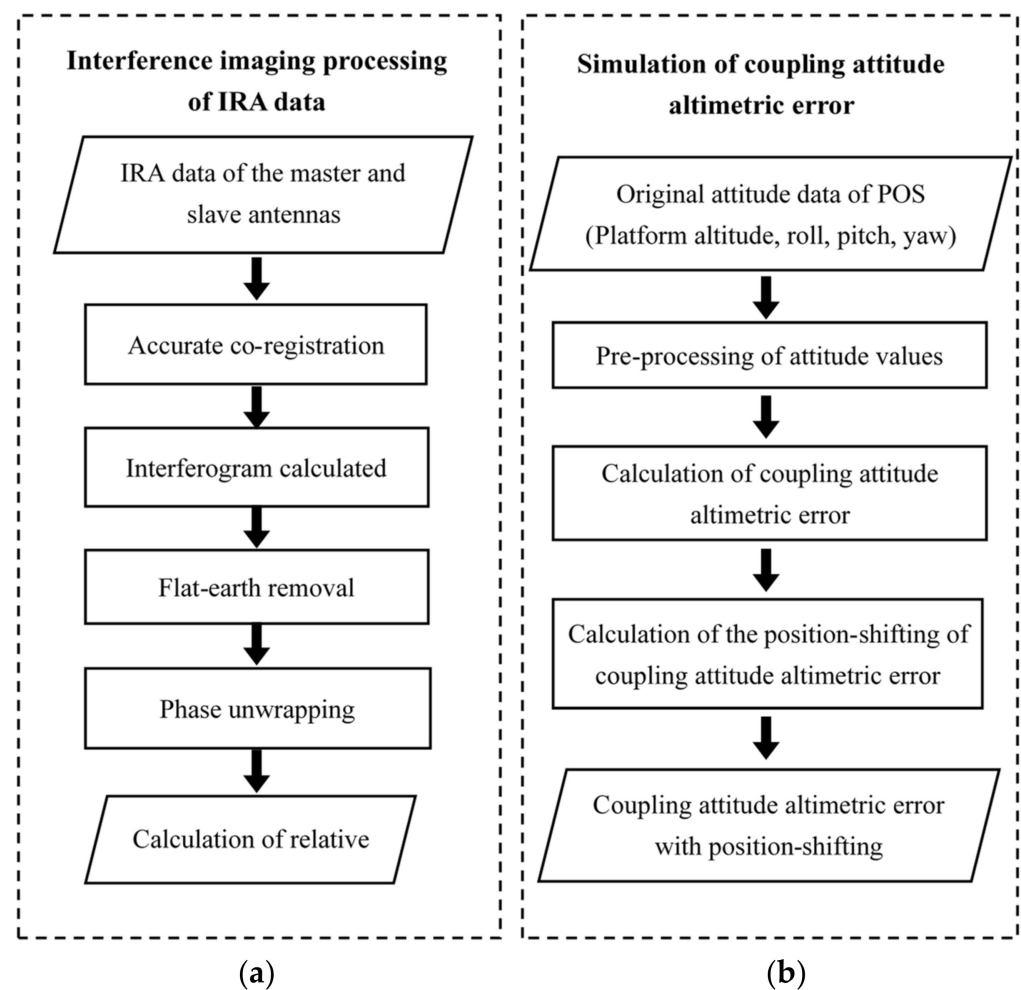
Parameters	Values
Center frequency	35 GHz
Aircraft altitude	3000 m
Azimuth resolution	0.3 m
Slant-range resolution	0.3 m
Beam width	1.36 deg
Airborne velocity	67 m/s (RZ14, RZ16) 83 m/s (RZ24)
Incidence angle	1~15 deg
Baseline length	0.3 m
Baseline orientation angle	−10 deg
Aircraft Heading angle	16 deg (RZ14) 15 deg (RZ16) 17 deg (RZ24)

Table 2. Pos_av610 absolute accuracy specifications.

Parameters	Values
Aircraft altitude	2~3 cm
Aircraft attitude angle	0.003 deg
Aircraft velocity	0.005 m/s

The airborne experimental data contains IRA data and systematic attitude data. In the calculation of relative SSE using the master–slave images acquired by the IRA, the systematic attitude errors are reflected in the interferometric phase. Since the interferometric phase contains the elevation phase and the flat-earth phase, and if the systematic attitude errors cannot be removed in the process of the flat-earth phase removal, this will finally lead to the coupling attitude altimetric error. The systematic attitude errors, which include platform altitude error, roll error, pitch error, and yaw error, are deviations of the attitude data between POS_AV610 and the nominal attitude values, and they can be used to simulate the generation process of altimetric error. The coupling attitude altimetric error and its position-shifting are calculated based on the theoretical formulas proposed in Section 2, and the simulated results will be compared with the relative SSE retrieved from IRA images.

The flow chart of the data processing is shown in Figure 4 [18,33–35].

**Figure 4.** Flowchart. (a) Relative SSE imaging processing. (b) Coupling attitude altimetric error calculation.

The master and slave images received by the airborne IRA during the three experiments are shown in Figure 5.

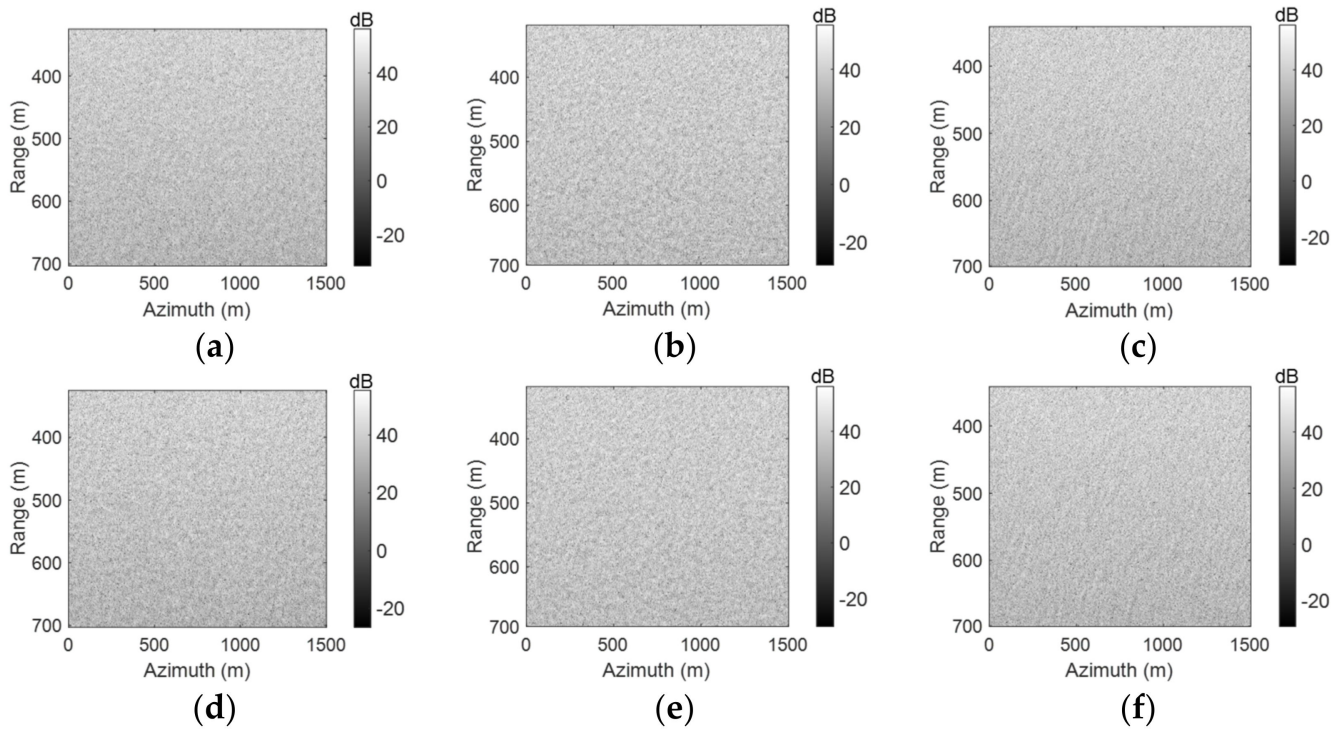


Figure 5. Master and slave IRA images. (a,d) Master and slave IRA images RZ14. (b,e) Master and slave IRA images of data RZ16. (c,f) Master and slave IRA images of data RZ24.

According to the process in Figure 4, the relative SSE images are retrieved from the experimental IRA images, and the results after the unified ground resolution processing are shown in Figure 6.

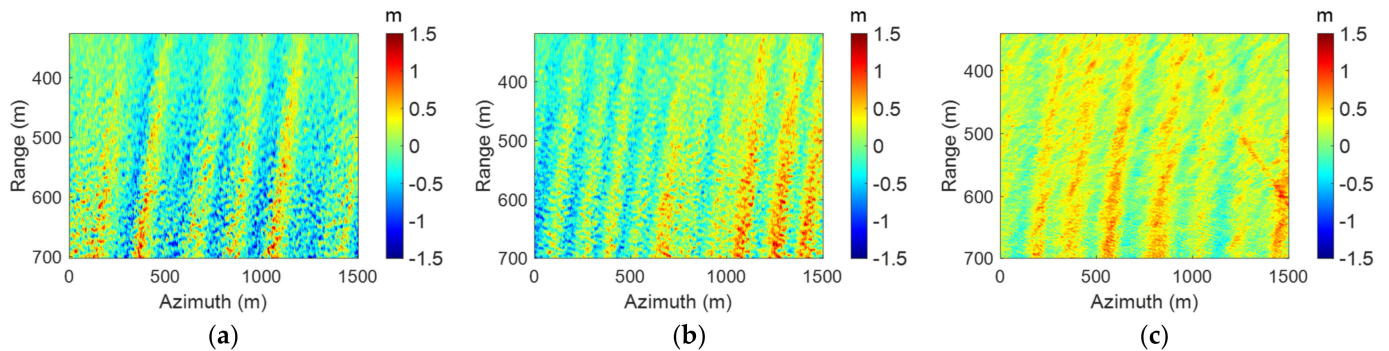


Figure 6. The relative SSE retrieved from IRA images. (a) RZ14. (b) RZ16. (c) RZ24.

From Figure 6, we can find that there are slant stripes in the retrieved SSE images. Along the azimuth direction of the IRA images, the stripes show variation characteristics of positive and negative oscillations and just like swells propagating approximately. However, along the range direction of the IRA images, it can be found that the amplitude of the oscillations all increase with ground range. This characteristic indicates that the slant stripes are not caused by sea surface swells.

In order to reveal the physical mechanism of the slant stripes in Figure 6, the coupling attitude altimetric errors induced by the systematic attitude errors of the airborne IRA are evaluated based on the theoretical formulas proposed in Section 2. The systematic attitude errors recorded by the POS_AV610 are shown in Figure 7.

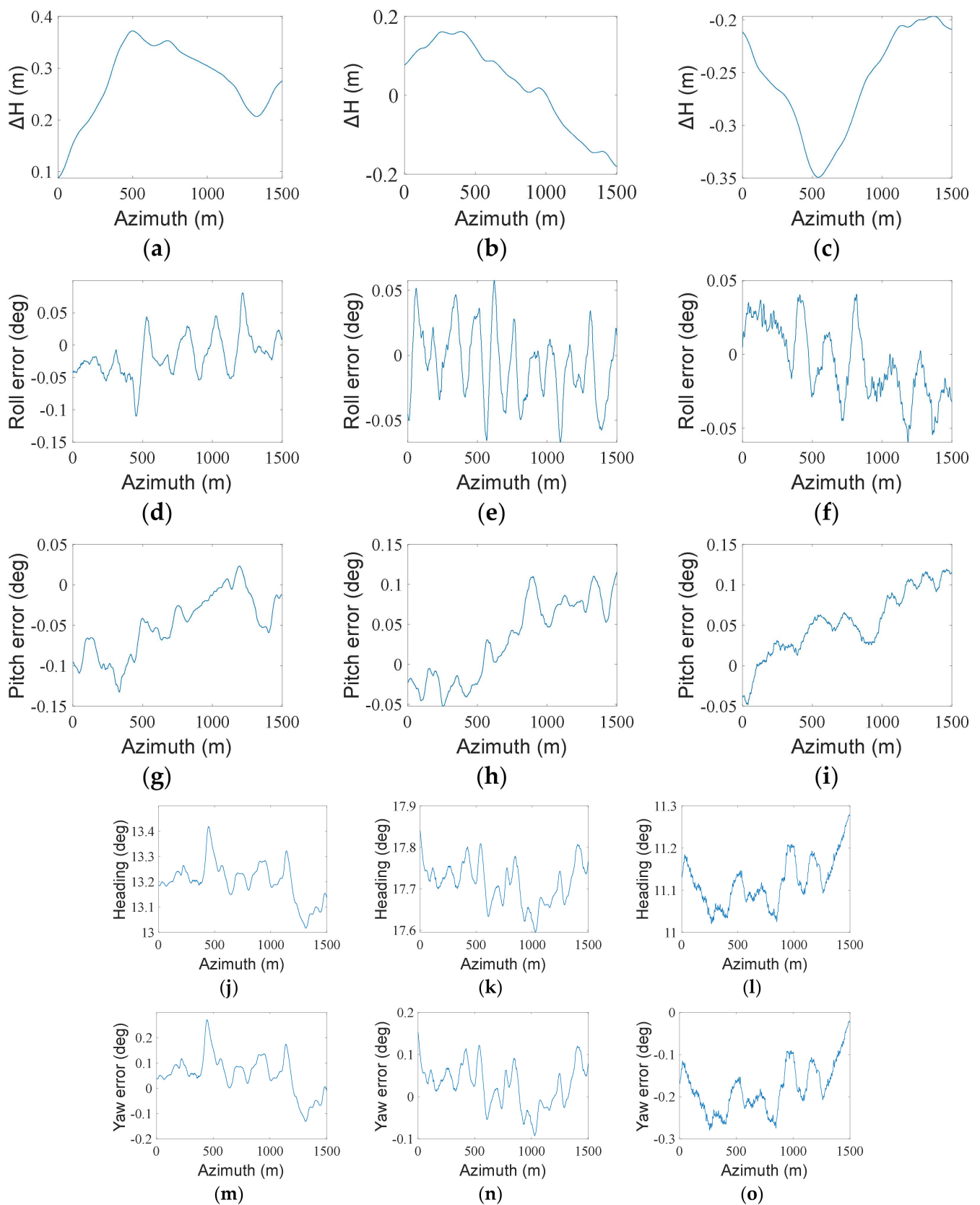


Figure 7. Attitude parameters of three data sets. (a,d,g,j,m) Platform altitude error, roll error, pitch error, heading angle, and yaw error of data RZ14. (b,e,h,k,n) Platform altitude error, roll error, pitch error, heading angle, and yaw error of data RZ16. (c,f,i,l,o) Platform altitude error, roll error, pitch error, heading angle, and yaw error of data RZ24.

Here, it should be pointed out that the systematic attitude errors in Figure 7 have been smoothed with a spatial window whose size is equal to the synthetic aperture scale of the IRA. As shown in Figure 7, although the variations of the platform altitude errors are significant, compared with the attitude angle errors, the altitude errors change slowly. The attitude angle errors have rapid changes, which are high-frequency errors compared to the platform altitude error. There is a fixed aircraft heading angle for each data set. As shown in Table 1, the aircraft heading angles of data RZ14, RZ16, and RZ24 are 16 degrees, 15 degrees, and 17 degrees, respectively, and the yaw error is floating around the aircraft heading angle, so the yaw angle error is the result of the yaw angle minus the fixed aircraft heading angle.

Based on the systematic attitude errors recorded by POS_AV610, the coupling attitude altimetric errors evaluated by Equation (13) are shown in Figure 8.

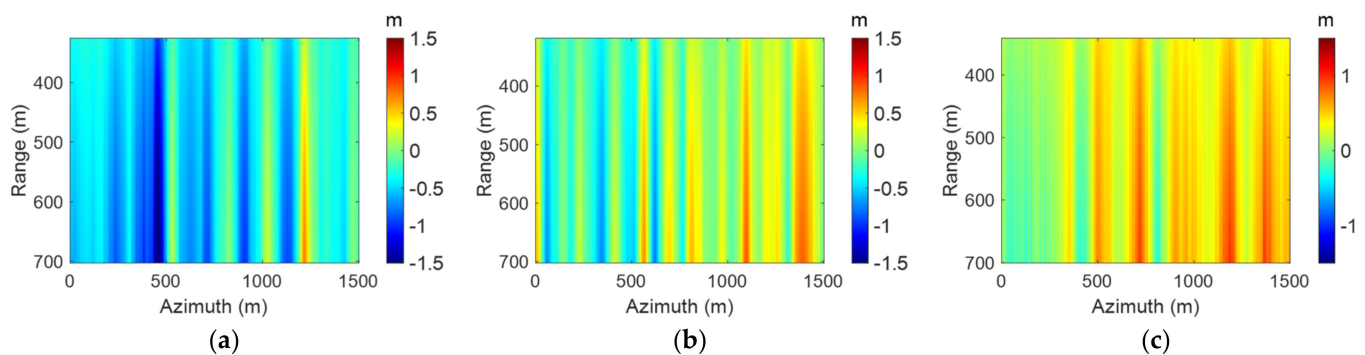


Figure 8. Coupling attitude altimetric errors without correction of the shift of imaging position. (a) RZ14. (b) RZ16. (c) RZ24.

As analyzed in Section 2, the platform altitude error theoretically causes an altimetric error that has an opposite variation and is fixed along the range direction, capable of reaching sub-meter level. The variation of the roll error along the azimuthal direction induces a positive and negative oscillation characteristic, and the spatial scale of the variation is consistent with the stripes in Figure 6. The altimetric error caused by the roll error increases along the range direction, and up to the meter level, which is the main source of the coupling attitude altimetric error. According to Equation (24), the altimetric error caused by the pitch error theoretically does not change along the range direction, and only at the centimeter level, which is a small contribution. According to Equation (26), the yaw error will cause no contribution to altimetric error theoretically. The coupling attitude altimetric errors evaluated by Equation (13) are strictly along the range direction of the IRA. However, as shown in Figure 6, the altimetric errors in the images acquired by the airborne IRA are all slanted along the range direction. As discussed in the previous section, the coupling attitude altimetric errors in Figure 8 need a position-shifting correction both along the range and the azimuth directions of the IRA image. According to Equation (28), the position-shifting is related to platform altitude, pitch, and yaw. The position-shifting along the azimuth and the range directions for each pixel in the swath of the IRA images are calculated, respectively, by Equation (28), and the results are shown in Figure 9.

The absolute values of the position-shifting along the range and azimuth directions are all increasing with ground range distance. In Figure 9a,c,e, the position-shiftings along the azimuth direction reach about 100 m at the far range of the IRA images. By contrast, in Figure 9b,d,f, the position-shiftings along the range direction are relatively smaller, only about 20 m, 30 m, and 14 m at the far range of the IRA images.

The results of the coupling attitude altimetric error with correction of position-shifting are shown in Figure 10.

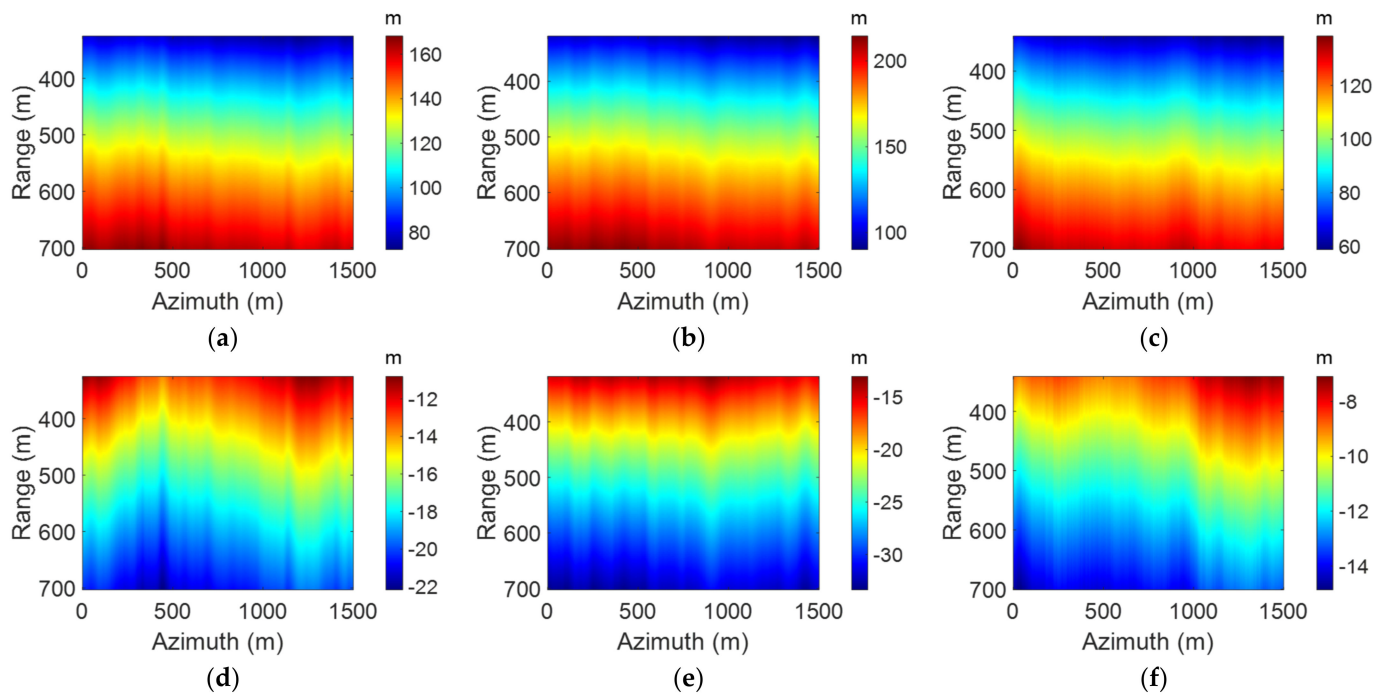


Figure 9. Position-shifting of coupling attitude altimetric errors. (a–c) The position-shifts along the azimuth direction (positive in the direction of flight). (d–f) The position-shifts along range direction (positive in the look direction) l in the images RZ14, RZ16, and RZ24.

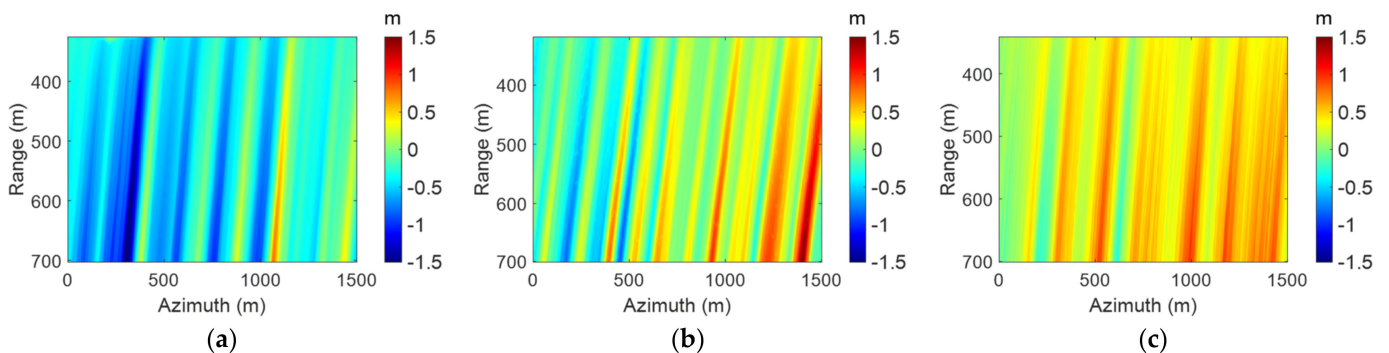


Figure 10. Coupling attitude altimetric errors with correction of position-shifting and resolution unifying of ground distance. (a) RZ14. (b) RZ16. (c) RZ24.

It can be seen that the features of the slant stripes in Figure 10 are consistent with those in Figure 6. To make a quantitative comparison, the profile curves of the altimetric error along the azimuth of the IRA images in Figure 10 are compared with the SSE retrieved from IRA images in Figure 6 at 3 different ranges (the nadir range at 50m, the middle range at 350 m, and the far range at 700 m). It should be clarified that in this comparison, the SSE retrieved from IRA images contain both geophysical signals and the altimetric errors. In order to show the high-frequency altimetric error more clearly, only the altimetric errors induced by the attitude angle errors are shown in Figure 11.

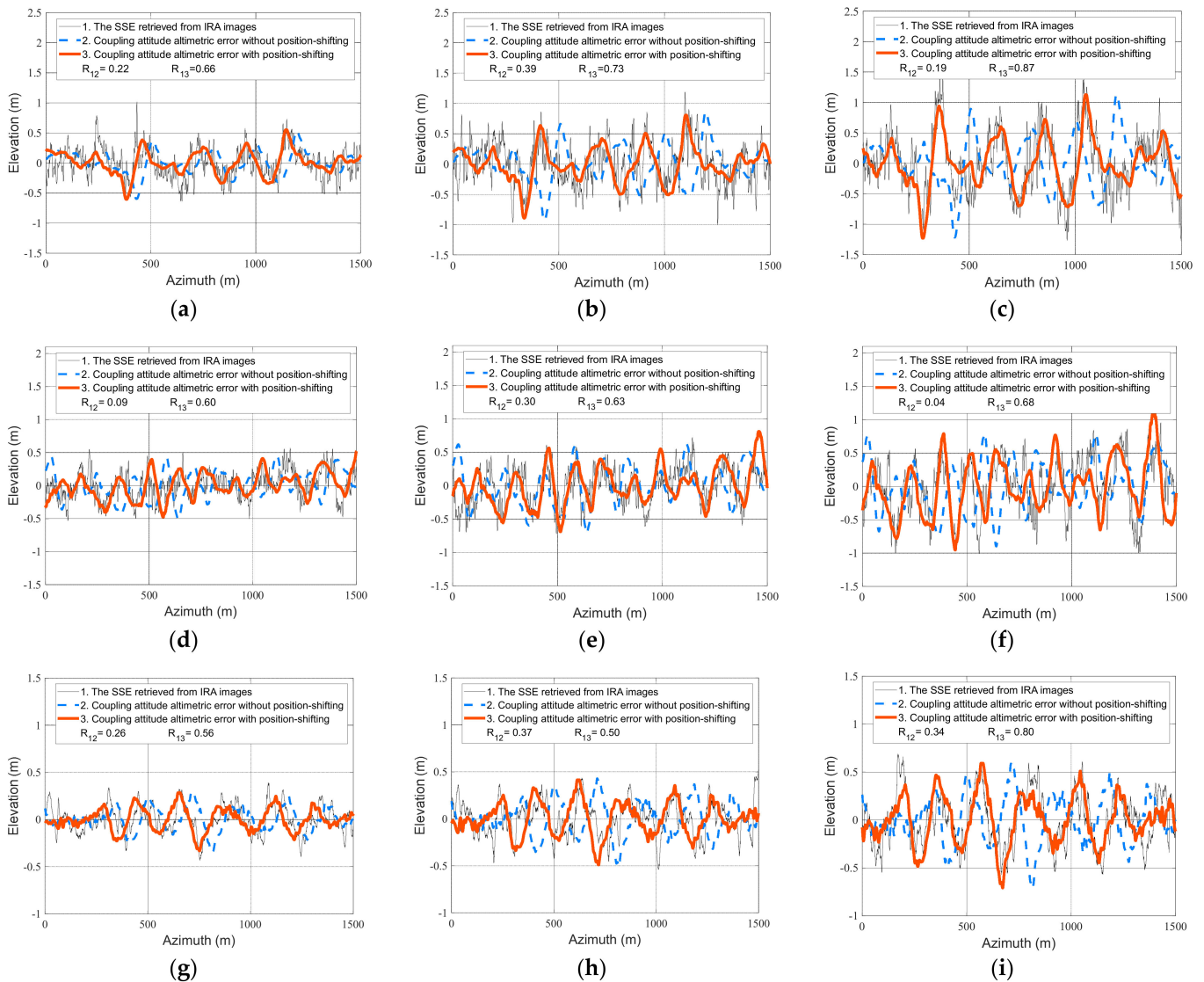


Figure 11. Profiles of the coupling attitude altimetric errors and the SSE retrieved from IRA images. R_{12} is the correlation coefficient of the SSE retrieved from IRA images (the thin black solid curves) and coupling attitude altimetric errors without position-shifting (the blue dashed curves), and R_{13} is the correlation coefficients of the SSE retrieved from IRA images and coupling attitude altimetric errors with position-shifting (the thick red solid curves). (a–c) are the profiles retrieved from RZ14 at the nadir range, middle range, and far range, respectively. (d–f) are the profiles retrieved from RZ16 at the nadir range, middle range, and far range, respectively. (g–i) are the profiles retrieved from RZ24 at the nadir range, middle range, and far range, respectively.

The thin black solid curves are the SSE retrieved from IRA images, the blue dashed curves denote the coupling attitude altimetric errors without position-shifting, and the thick red solid curves are the coupling attitude altimetric errors when the position-shifting is corrected. According to Equation (13) and the analyses in Section 2.2, the altimetric errors increase with the increasing ground range, and the position-shifting of them is also changing. It can be seen from Table 3, the high correlation coefficients R_{13} mean that the coupling attitude altimetric errors with position-shifting matched well with the measurements, in spite of the effects of the sea surface wind waves and the random phase noise. The correlation coefficients R_{13} also increase with the ground range because the SSE retrieved from IRA images includes both geophysical signals and all kinds of error signals, and the further away from the nadir point, the greater the contribution of altimetric errors

to the elevation measurements. The altimetric errors at the far range are the major features of the elevation measurements, which makes the higher correlation coefficient. However, if the position-shifting is neglected, as shown in Figure 11, the theoretical coupling attitude altimetric errors are not consistent with the SSE retrieved from IRA images. It can be found from Table 3 that the correlation coefficients R_{12} are all less than 0.40 and the minimum one is reduced to 0.04. This result means that the position-shifting caused by pitch and yaw must be considered when we analyze or correct the IRA altimetric errors induced by the systematic attitude errors.

Table 3. The correlation coefficients of the SSE retrieved from IRA images and coupling attitude altimetric errors.

The Correlation Coefficients	RZ14		RZ16		RZ24	
	R_{12}	R_{13}	R_{12}	R_{13}	R_{12}	R_{13}
At the nadir range (50 m)	0.22	0.66	0.09	0.60	0.26	0.56
At the middle range (350 m)	0.39	0.73	0.30	0.63	0.37	0.50
At the far range (700 m)	0.19	0.87	0.04	0.68	0.34	0.80

The main reason why the coupling attitude altimetric errors cannot be perfectly matched with the SSE retrieved from the IRA images could be that the coupling attitude altimetric errors are calculated by using the instantaneous attitude errors recorded by the POS, while the IRA images are obtained by the integration process of synthetic aperture. On the other hand, the SSE retrieved from IRA images include not only geophysical signals and altimetric error signals but also signals of surface wind waves and other noises.

4. Conclusions

The systematic attitude errors of the IRA contain four main aspects: platform altitude error, roll error, pitch error, and yaw error. The independent analysis of each error can qualitatively and quantitatively illustrate their influence on the altimetric error. However, for the real observations of the altimeter, the altimetric error induced by the systematic attitude error is coupled together. In addition, the position-shifting of the altimetric error induced by the attitude error of the platform is non-negligible in the IRA measurement, although this problem has not attracted extensive attention in the scientific community. In this paper, the theoretical formulas for the coupling attitude altimetric error were derived and verified using the airborne IRA experiments. Based on theoretical formulas, the coupling attitude altimetric error was evaluated by using the attitude data measured by the airborne POS. The comparisons illustrated that the altimetric error induced by attitude error could be well calculated by the theoretical formulas proposed by this study. In addition, the attitude errors of the IRA are coupled together, and, therefore, it is not possible to reduce the coupling attitude altimetric error by correcting the altitude, roll, pitch, or yaw errors independently. Since the coupling attitude altimetric error is calculated using the instantaneous attitude errors, which is different from the IRA images obtained by the integration process of synthetic aperture, it still poses a challenge to obtain the geophysical signal by directly subtracting the coupling attitude altimetric errors from the SSE retrieved from airborne IRA images, and this will be further discussed in the future works.

The theoretical formulas obtained in this work are of significance to the analysis and elimination of IRA and the systematic altimetry error induced by attitude errors.

Author Contributions: Conceptualization, Y.W. and C.Z.; methodology, H.T. and Y.W.; formal analysis, H.T., Y.W. and D.S.; data curation, H.S.; writing—original draft preparation, H.T.; writing—review and editing, H.T., Y.W. and C.Z.; funding acquisition, Y.W., C.Z. and G.C. All authors have read and agreed to the published version of the manuscript.

Funding: This research was funded by the National Nature Science Foundations of China under Grant 41976167, the National Nature Science Foundation of China under Grant 42030406, and the Marine S&T Fund of Shandong Province for Pilot National Laboratory for Marine Science and Technology (Qingdao) under Grant 2018SDKJ0102-8.

Data Availability Statement: The airborne IRA images were provided by the No.23 Research Institute of the Second Academy of China Aerospace Science and Industry Corporation, and the GNSS buoy data was provided by the Marine Survey Research Center, First Institute of Oceanography, Ministry of Natural Resources.

Conflicts of Interest: The authors declare no conflict of interest.

References

- Rodriguez, E.; Pollard, D.; Martin, M. Wide-Swath Ocean Altimetry Using Radar Interferometry. *IEEE Trans. Geosci. Remote Sens.* **1999**, *37*, 624–626. Available online: <https://dataverse.jpl.nasa.gov/dataset.xhtml?persistentId=hdl:2014/17962> (accessed on 23 October 2022).
- Fu, L.-L.; Chelton, D.B.; Le Traon, P.-Y.; Morrow, R. Eddy Dynamics from Satellite Altimetry. *Oceanography* **2010**, *23*, 14–25. [\[CrossRef\]](#)
- Fu, L.-L.; Alsdorf, D.; Rodriguez, E.; Morrow, R.; Mognard, N.; Lambin, J.; Vaze, P.; Lafon, T. The SWOT (Surface Water and Ocean Topography) Mission: Spaceborne Radar Interferometry for Oceanographic and Hydrological Applications. *Proc. Oceanobs* **2009**, *9*, 21–25.
- Esteban-Fernandez, D.; Fu, L.-L.; Rodriguez, E.; Brown, S.; Hodges, R. Ka-Band SAR Interferometry Studies for the SWOT Mission. In Proceedings of the 2010 IEEE International Geoscience and Remote Sensing Symposium, Honolulu, HI, USA, 25–30 July 2010; pp. 4401–4402. [\[CrossRef\]](#)
- Chen, G.; Tang, J.; Zhao, C.; Wu, S.; Yu, F.; Ma, C.; Xu, Y.; Chen, W.; Zhang, Y.; Liu, J.; et al. Concept Design of the “Guanlan” Science Mission: China’s Novel Contribution to Space Oceanography. *Front. Mar. Sci.* **2019**, *6*, 194. [\[CrossRef\]](#)
- Fu, L.-L.; Ubelmann, C. On the Transition from Profile Altimeter to Swath Altimeter for Observing Global Ocean Surface Topography. *J. Atmos. Ocean. Technol.* **2014**, *31*, 560–568. [\[CrossRef\]](#)
- Fjørtoft, R.; Koudogbo, F.; Duro, J.; Ruiz, C.; Gaudin, J.-M.; Mallet, A.; Pourthie, N.; Lion, C.; Ordoqui, P.; Arnaud, A. *KaRIn on SWOT: Modeling and Simulation of Near-Nadir Ka-Band Interferometric SAR Images*; SPIE: Toulouse, France, 2010; Volume 7826, pp. 306–314. [\[CrossRef\]](#)
- Fjørtoft, R.; Gaudin, J.-M.; Pourthie, N.; Lalaurie, J.-C.; Mallet, A.; Nouvel, J.-F.; Martinot-Lagarde, J.; Oriot, H.; Borderies, P.; Ruiz, C.; et al. KaRIn on SWOT: Characteristics of Near-Nadir Ka-Band Interferometric SAR Imagery. *IEEE Trans. Geosci. Remote Sens.* **2014**, *52*, 2172–2185. [\[CrossRef\]](#)
- Parrinello, T.; Shepherd, A.; Bouffard, J.; Badessi, S.; Casal, T.; Davidson, M.; Fornari, M.; Maestroni, E.; Scagliola, M. CryoSat: ESA’s Ice Mission—Eight Years in Space. *Adv. Space Res.* **2018**, *62*, 1178–1190. [\[CrossRef\]](#)
- Gray, L.; Burgess, D.; Copland, L.; Cullen, R.; Galin, N.; Hawley, R.; Helm, V. Interferometric Swath Processing of Cryosat-2 Data for Glacial Ice Topography. *Remote Sens.* **2013**, *7*, 3133–3162. [\[CrossRef\]](#)
- Galín, N.; Wingham, D.J.; Cullen, R.; Francis, R.; Lawrence, I. Measuring the Pitch of CryoSat-2 Using the SAR Mode of the SIRAL Altimeter. *IEEE Geosci. Remote Sens. Lett.* **2014**, *11*, 1399–1403. [\[CrossRef\]](#)
- Gourmelen, N.; Escorihuela, M.J.; Shepherd, A.; Foresta, L.; Muir, A.; Garcia-Mondéjar, A.; Roca, M.; Baker, S.G.; Drinkwater, M.R. CryoSat-2 Swath Interferometric Altimetry for Mapping Ice Elevation and Elevation Change. *Adv. Space Res.* **2018**, *62*, 1226–1242. [\[CrossRef\]](#)
- Esteban Fernandez, D.; Pollard, B.; Vaze, P.; Abelson, R. SWOT Project Mission Performance and Error Budget. *Jet Propuls. Lab. Doc. D-79084 Revis. A.* 2017. Available online: https://swot.jpl.nasa.gov/system/documents/files/2178_2178_SWOT_D-79084_v10Y_FINAL_REVA_06082017.pdf (accessed on 23 October 2022).
- Rodriguez, E.; Pollard, B. *Centimetric Sea Surface Height Accuracy Using the Wide-Swath Ocean Altimeter*; IEEE: Toulouse, France, 2003; Volume 5, pp. 3011–3013. [\[CrossRef\]](#)
- Moccia, A.; Vetrilla, S. A Tethered Interferometric Synthetic Aperture Radar (SAR) for a Topographic Mission. *IEEE Trans. Geosci. Remote Sens.* **1992**, *30*, 103–109. [\[CrossRef\]](#)
- Phalippou, L.; Guijarro, J. *End to End Performances of a Short Baseline Interferometric Radar Altimeter for Ocean Mesoscale Topography*; IEEE: Anchorage, AK, USA, 2004; Volume 2, pp. 765–768. [\[CrossRef\]](#)
- Rosen, P.A.; Hensley, S.; Joughin, I.R.; Li, F.K.; Madsen, S.N.; Rodriguez, E.; Goldstein, R.M. Synthetic Aperture Radar Interferometry. *Proc. IEEE* **2000**, *88*, 333–382. [\[CrossRef\]](#)
- Shao, Y.; Zhu, Z. *Studies of Spaceborne Interferometric Synthetic Aperture Radars*; SPIE: Barcelona, Spain, 1996; Volume 2757, pp. 443–449.
- Le Hénaff, M.; De Mey, P.; Mourre, B.; Le Traon, P.-Y. Contribution of a Wide-Swath Altimeter in a Shelf Seas Assimilation System: Impact of the Satellite Roll Errors. *J. Atmos. Ocean. Technol.* **2008**, *25*, 2133–2144. [\[CrossRef\]](#)
- Zhang, Y.; Zhai, W.; Gu, X.; Shi, X.; Kang, X. *Experimental Demonstration for the Attitude Measurement Capability of Interferometric Radar Altimeter*; Warsaw University of Technology (WUT): Gdansk, Poland, 2014; pp. 1–4. [\[CrossRef\]](#)

21. Sun, D.; Wang, Y.; Bai, Y.; Zhang, Y. *Ocean Waves Inversion Based on Airborne Radar Images with Small Incident Angle*; IEEE: Hangzhou, China, 2020; pp. 1–4. [[CrossRef](#)]
22. Sun, D.; Zhang, Y.; Wang, Y.; Chen, G.; Sun, H.; Yang, L.; Bai, Y.; Yu, F.; Zhao, C. Ocean Wave Inversion Based on Airborne IRA Images. *IEEE Trans. Geosci. Remote Sens.* **2021**, *60*, 1–13. [[CrossRef](#)]
23. Mallorqui, J.J.; Bara, M.; Broquetas, A. *Calibration Requirements for Airborne SAR Interferometry*; SPIE: Barcelona, Spain, 2000; Volume 4173, pp. 267–278. [[CrossRef](#)]
24. Gao, L.; Sun, H.; Qi, J.; Jiang, Q. Effect of Random Phase Error and Baseline Roll Angle Error on Eddy Identification by Interferometric Imaging Altimeter. *J. Oceanol. Limnol.* **2021**, *40*, 1881–1888. [[CrossRef](#)]
25. Angino, G.; Impagnatiello, F.; Zelli, C. *High Spatial Resolution Radar Altimetry for Global Earth Topography Mapping*; IEEE: Singapore, 1997; Volume 1, pp. 15–17. [[CrossRef](#)]
26. Fu, L.-L.; Alsdorf, D.; Morrow, R.; Rodriguez, E.; Mognard, N. *SWOT: The Surface Water and Ocean Topography Mission: Wide-Swath Altimetric Elevation on Earth*; Jet Propulsion Laboratory, National Aeronautics and Space Administration: Pasadena, CA, USA, 2012. Available online: <https://dataverse.jpl.nasa.gov/dataset.xhtml?persistentId=hdl:2014/41996> (accessed on 23 October 2022).
27. Galin, N.; Wingham, D.J.; Cullen, R.; Fornari, M.; Smith, W.H.F.; Abdalla, S. Calibration of the CryoSat-2 Interferometer and Measurement of Across-Track Ocean Slope. *IEEE Trans. Geosci. Remote Sens.* **2013**, *51*, 57–72. [[CrossRef](#)]
28. Liu, B.; Zhang, R.; Wan, X.; Li, Y.; Yuan, S. Accuracy Analysis of Multi-base InSAR Altimeter in Ocean Surface Relative Elevation Measurement. *J. Eng.* **2019**, *2019*, 5789–5792. [[CrossRef](#)]
29. Rodriguez, E.; Martin, J.M. Theory and Design of Interferometric Synthetic Aperture Radars. In *IEE Proceedings F (Radar and Signal Processing)*; IET Digital Library: Stevenage, UK, 1992; Volume 139, pp. 147–159. [[CrossRef](#)]
30. Enjolras, V.; Vincent, P.; Souyris, J.-C.; Rodriguez, E.; Phalippou, L.; Cazenave, A. Performances Study of Interferometric Radar Altimeters: From the Instrument to the Global Mission Definition. *Sensors* **2006**, *6*, 164–192. [[CrossRef](#)]
31. Hanssen, R.F. *Radar Interferometry: Data Interpretation and Error Analysis*; Springer Science & Business Media: Berlin/Heidelberg, Germany, 2001; Volume 2.
32. Kutoglu, H.S.; Mekik, C.; Akcin, H. A Comparison of Two Well Known Models for 7- Parameter Transformation. *Aust. Surv.* **2002**, *47*, 24–30. [[CrossRef](#)]
33. Yang, L.; Xu, Y.; Zhou, X.; Zhu, L.; Jiang, Q.; Sun, H.; Chen, G.; Wang, P.; Mertikas, S.P.; Fu, Y.; et al. Calibration of an Airborne Interferometric Radar Altimeter over the Qingdao Coast Sea, China. *Remote Sens.* **2020**, *12*, 1651. [[CrossRef](#)]
34. Birkett, C.M. Contribution of the TOPEX NASA Radar Altimeter to the Global Monitoring of Large Rivers and Wetlands. *Water Resour. Res.* **1998**, *34*, 1223–1239. [[CrossRef](#)]
35. Wu, X.; Hensley, S.; Rodriguez, E.; Moller, D.; Muellerschoen, R.; Michel, T. Near Nadir Ka-Band Sar Interferometry: SWOT Airborne Experiment. In *Proceedings of the 2011 IEEE International Geoscience and Remote Sensing Symposium, Vancouver, BC, Canada, 24–29 July 2011*; pp. 2681–2684. [[CrossRef](#)]